Acta Materialia 257 (2023) 119163

Contents lists available at ScienceDirect

Acta Materialia

journal homepage: www.elsevier.com/locate/actamat

Full length article

$CoFeNiTi_x$ and $CrFeNiTi_x$ high entropy alloy thin films microstructure formation

Aoyan Liang [a], Daniel C. Goodelman [b], Andrea M. Hodge [a,b], Diana Farkas [c], Paulo S. Branicio [a,*]

[a] Mork Family Department of Chemical Engineering and Materials Science, University of Southern California, Los Angeles, CA 90089, United States
[b] Department of Aerospace and Mechanical Engineering, University of Southern California, Los Angeles, CA 90089, United States
[c] Department of Materials Science & Engineering, Virginia Polytechnic Institute and State University, Blacksburg, VA 24061, United States

ARTICLE INFO

Keywords:
High entropy alloy
Thin films
Phase stability
Molecular dynamics
Average atom
Model
Physical vapor deposition

ABSTRACT

High entropy alloys (HEA) composition-structure relationships are crucial for guiding their design and applications. Here, we use a combined experimental and molecular dynamics (MD) approach to investigate phase formation during physical vapor deposition (PVD) of $CoFeNiTi_x$ and $CrFeNiTi_x$ HEA thin films. We vary titanium molar ratio from 0 to 1 to understand the role of a larger element in the alloy mixture. The experiments show that a high titanium content favors amorphous phase formation in the samples produced by magnetron co-sputtering. In contrast, a low titanium content results in the formation of a face-centered cubic (FCC) structure in both HEA families. This effect of titanium content on the stability of the amorphous and FCC phases is reproduced in PVD MD simulations. The threshold titanium molar ratio is identified to be ~0.53 and ~0.16 for the $CoFeNiTi_x$ and $CrFeNiTi_x$ films in the experiments, and ~0.53 and ~0.53 in the MD simulations. In addition, the atomistic modeling allows for energy versus volume calculations with increasing titanium content, which demonstrate the stabilization of the amorphous phase with respect to crystalline structures. To isolate the effect of atomic sizes, additional simulations are performed using an average-atom model, which disregards differences in atomic radii while preserving the average properties of the alloy. In these simulations, the energetic stability of the amorphous phase disappears. The combined experimental and simulation results demonstrate that the formation of the amorphous phase in HEA thin films generated by PVD is directly caused by the atomic size difference.

1. Introduction

High entropy alloy (HEA), also referred to as compositionally complex alloy and multi-principal element alloy, is a novel idea for alloy design based on combinations of multiple principal elements that has been attracting considerable interest since it was proposed in 2004 [1–3]. HEAs exhibit many exceptional properties such as excellent fatigue resistance and toughness, a good balance between strength and elasticity, high oxidation and corrosion resistance, and distinct electrical and magnetic properties [4–9]. However, due to the vast number of possible HEA compositions, exploring the composition-structure relationships became one of the biggest challenges in the field [10,11]. Traditional bulk HEA synthesis methods such as arc-melting, plasma sintering, and mechanical alloying are not suitable for investigating the enormous and multidimensional composition space of HEAs [12,13]. A high-throughput and accelerated synthesis technique such as physical vapor deposition (PVD) is sought after to enable a swift navigation and screening of HEA compositions [11].

Magnetron sputtering is a commonly used PVD technique for the synthesis of HEA thin films, featuring a relatively low synthesis cost and excellent tunability of film composition [13]. Previous studies have shown that HEA thin films display comparable or even "enhanced" mechanical and magnetic properties than their bulk counterparts [14–18]. For example, the $CoCrFeNiAl_{0.3}$ thin film prepared by magnetron sputtering exhibits a similar elastic modulus as its bulk counterpart yet a four times higher hardness due to the nanocrystalline structure of the thin film [14]. Nonetheless, the phase formation of HEAs is potentially different in sputtered thin films compared to bulk because of the fast-cooling rate inherent to the sputtering deposition process, which largely suppresses atomic diffusion [13,19]. Kube et al. [12] suggested that an increased cooling rate reduces the phase complexity in as-sputtered HEA thin films, ultimately leaving a single solid solution (SS) phase, facilitating the observation of the phase preference for a given HEA composition.

* Corresponding author.
E-mail address: branicio@usc.edu (P.S. Branicio).

https://doi.org/10.1016/j.actamat.2023.119163
Received 6 January 2023; Received in revised form 22 May 2023; Accepted 12 July 2023
Available online 16 July 2023

The phase formation in HEAs is also influenced by the specific chemical composition of the alloy. Recent studies have demonstrated that the addition of alloy elements with relatively large ionic radii leads to a large atomic size difference in the alloy, resulting in changes in phase stability in both bulk and thin film HEAs [9,12,17,18,20–25]. For instance, some studies have shown that the presence of Al enhances the stability of the body-centered cubic (BCC) structure in HEAs, which often results in a face-centered cubic (FCC) to BCC phase transition with increasing Al content [12,25]. Other studies indicate that an increased Ti or Nb content favors the formation of an amorphous structure [17, 18]. These discrepancies among the roles of different large alloy elements highlights the need to understand the effects of each element and the role of atomic size difference on the phase stability and microstructure formation of HEAs. In addition, since the conventional Hume-Rothery rules are insufficient for the HEA phase prediction, more predictive models are desired to investigate the phase formation mechanisms and the competition between different phases in HEAs [3]. For example, Zhang et al. [26] proposed a phase formation rule for HEAs, where a system with a larger atomic size difference and largely negative enthalpy of mixing favors an amorphous structure. This model was further improved by including the entropy of mixing, providing an appropriate criterion to separate amorphous and SS phases [27].

Molecular dynamics (MD) simulations are well suited for the investigation of film growth mechanisms and phase stability of such complex multi-element HEA films by direct simulation of the PVD process [28–31]. Few studies have simulated the deposition process of HEA films towards understanding their microstructure formation [13,32–34]. This may be due to the lack of accurate and robust force fields that represent the complex interaction among multiple alloy elements. Recently, an embedded atom model (EAM) potential was developed enabling the representation of different HEA systems [35,36], making possible the investigation of phase stability and microstructure formation during the PVD process.

In this work, we employ experiments and MD simulations of the PVD process to investigate microstructure formation in two common HEA families, CoFeNiTi$_x$ and CrFeNiTi$_x$, where x is the molar ratio of Ti. Our goal is to understand the effects of adding increasing amounts of a larger element to the mixtures of similarly sized component in HEAs. Simulation results indicate phase stability trends are in good agreement with the experiments. By adjusting x from 0 to 1, the effect of Ti content on the phase formation in HEA films is revealed. In general, high Ti content induces a change in phase stability from FCC to amorphous. The presence of hexagonal close packed (HCP) and BCC is negligible in the samples considered. We also illustrate the phase stabilities of FCC, BCC, HCP, and amorphous structures for various compositions through energy versus volume calculations. Additional simulations using an average-atom (AA) potential that has similar overall properties yet averaged out local compositional and size fluctuations are performed to uncover the significant impact of the atomic size difference on the microstructure formation.

2. Methodology

2.1. Experimental methods

Samples are synthesized using DC magnetron co-sputtering from a high purity, single element Ti (99.995%) target and vacuum arc melted ternary alloy CrFeNi (99.9%) and CoFeNi (99.9%) targets (Plasmaterials, Inc.). A two-source sputtering system is used to co-sputter the single element Ti target with one of the ternary alloy targets onto 25 mm diameter Si (100) substrates to produce either CoFeNiTi or CrFeNiTi films. Sputtering powers are selected such that the nominal expected composition values for each alloying element are within the necessary defined range for HEAs. Deposition rates are between 0.18 and 0.24 nm/s. The resulting samples have a thickness of ~1 μm, measured using an AMBiOS XP-2 profilometer. Additional details about the sputtering conditions are provided in Tables SI and SII, in the Supplementary Materials. Because the CrFeNi target has a lower sputtering rate than that of the CoFeNi target, a higher Ti rate is required for CrFeNiTi$_x$ in order to match the compositions studied across both systems, as deposition power directly affects composition.

The elemental compositions of each sample are characterized by scanning electron microscopy/energy dispersive X-ray spectroscopy (SEM/EDS) (FEI Helios G4 P-FIB) at 20 kV. Top-surface micrographs are acquired via SEM using a beam current of 0.2 nA and an accelerating voltage of 5 kV. X-ray diffraction (XRD) with Cu Kα radiation is employed to acquire scans over a 2θ range from 30° to 90° or to 100° depending on the system of samples, with a step size of 0.05°/sec and a sampling rate of 1°/min using a Bruker D8 Advance Diffractometer.

2.2. Interatomic potential and the average-atom potential for the HEA alloy

A model EAM [37] interatomic potential is used for the HEA simulations [38]. These potentials represent model interactions that can be used to study trends in the alloy behavior properties. While these model interactions cannot be accurate in representing a particular alloy, they are the ideal way of studying various trends, helping understand exactly how certain material parameters influence overall properties. The particular potential set used here is for a five-component alloy in an FCC structure. The parameters used are chosen to resemble basic elastic and thermodynamic properties and size mismatches of FCC mixtures in the Fe-Ni-Cr-Co-Ti quinary system. The first four components Fe-Ni-Cr-Co are characterized by very similar atomic sizes and very small binary heats of mixing [39]. The method for generating the potential is similar to those used in previous work [40], yet based on FCC phases being stable for all pure components. The details of the potential for the four components of similar sizes are reported in detail in [38].

In contrast, the fifth element in the set used here is characterized by a significantly larger size. The fitting procedure for the pure Ti potential and mixed interactions used here is similar to the framework developed on our previous work involving the addition to the larger element Al to a set of potentials for elements of similar sizes. For all component elements, we use a set of cubic splines and a fitting algorithm designed to reproduce desired values of a, E, B, C_{11}, C_{12}, unrelaxed vacancy formation energy, SFE, and surface energies, in the FCC phase for all the five pure elements. The procedure ensured that the FCC structure has the lowest energy for all five-component elements when pure. For the case of FCC Ni these data are their actual experimental properties. For Fe, the target data are obtained from the values known for austenite, predicting an FCC phase stable at 0 K. For the FCC phases of Cr and Co the data are taken from available first-principle calculations. The potentials are developed in the effective pair scheme, with the derivative of the embedding function equal to 0, and electronic density equal to 1 (in arbitrary units), for the perfect lattice at the equilibrium lattice constant.

Table 1 lists the basic properties given by the potentials for the five

Table 1
Basic characteristics of the five component potentials used in the present work.

	(Fe)	(Ni)	(Cr)	(Co)	(Ti)
a (Å)	3.56	3.52	3.53	3.55	4.17
E (eV/atom)	4.40	4.45	4.20	4.41	4.85
B (eV/Å^3)	1.06	1.13	1.00	1.35	1.20
C11 (eV/Å^3)	1.19	1.54	1.24	1.65	1.91
C12 (eV/Å^3)	1.00	0.92	0.88	1.20	0.84
C44 (eV/Å^3)	0.48	0.78	0.70	0.89	0.51
Unrelaxed SF (mJ/m^2)	43	129	41	41	20
E $_{Vac}$ (eV)	1.61	1.61	1.41	1.36	1.54
Ebcc-Efcc (eV/atom)	0.11	0.15	0.10	0.08	0.23
Ehcp-Efcc (eV/atom)	0.01	0.02	0.01	0.01	0.01
(110) Surface energy (J/m^2)	2.00	2.05	2.02	2.08	1.76
(100) Surface energy (J/m^2)	1.86	1.88	1.88	1.90	1.75
(111) Surface energy (J/m^2)	1.70	1.75	1.65	1.60	1.56

elements in the set developed. There is a significant variation among the properties in the values of the SFE. As far as size, Ti is significantly larger than the other four components, as seen in the lattice parameter differences. Fig. 1 shows the pair components of the potentials developed for the pure components. The larger size of Ti is also evident from the position of the minimum in the pair functions. For the mixed pair interactions not involving Ti, the mixed pair functions are obtained as a simple average of the component pairs in order to represent very small heats of mixing. This procedure also results in very small deviations from Vegard's law. For the mixed pair interactions involving Ti we follow a procedure similar to that used in the addition of Al to the Fe-Ni-Cr-Co set [35]. In this scheme, the cross potentials M-Ti are obtained as a mix of one part of the Ti-Ti pair function and four parts of the M-M pair function of the other element.

Table 2 lists the properties obtained for the ten random FCC equiatomic binary compounds. All the binary random alloys not involving Ti do indeed have small heats of solution and small deviations from Vegard's law. The binaries involving Ti present much larger values. In the random configuration the heats of solution for binary mixtures containing Ti are positive deviations of ideality. This can be rationalized due to the larger size of the Ti atom, noting that in random configurations nearest neighbor Ti-Ti pairs will be present. This is also associated with the large deviations from Vegard's law observed for the random alloys containing Ti. As with the addition of the larger Al atom, the alloys containing Ti will have a strong tendency to order, avoiding nearest neighbor Ti-Ti pairs of larger atoms. To illustrate this, Table 3 lists the results for one possible ordered equiatomic alloy structure, the BCC based B2 structure where nearest neighbor Ti-Ti pairs are not present. These compounds are all predicted to more stable than the random FCC structure, as indicated by the more negative cohesive energy values.

Using a multi-species interatomic potential as a starting point, it is possible to determine a consistent single element potential representative of a given (random) alloy composition. A technique for developing this single element average potential is given by Varvenne and co-workers [41] and is referred to as the AA potential. The important feature of their technique is that the average atom material has averaged out all the local compositional and structural fluctuations of the random alloy, while critical average properties are the same as in the random alloy. By comparing material behavior computed for the average and actual random alloys, it is possible to isolate the effects of the local random compositional fluctuations. Varvenne and co-workers [41] showed that the AA potential can be quantitatively accurate for a wide range of random alloy properties. Here we have followed their method to derive the AA potential corresponding to the quinary HEA alloys of various compositions addressed here.

2.3. Simulation details

MD simulations are performed using LAMMPS [42]. All HEA thin films are deposited on an FCC Ni (100) substrate with a 3.52 Å lattice

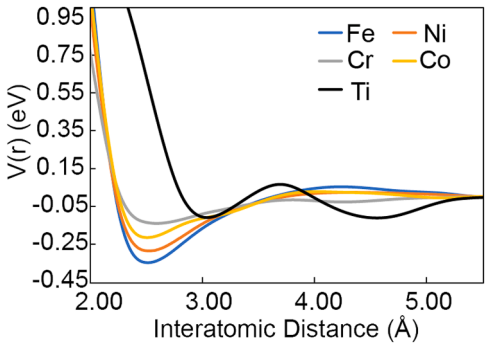

Fig. 1. The pair component of the potentials used here for the five components.

Table 2
Properties of the binary FCC random equiatomic mixtures as given by the potentials used in this work.

Binary random Alloy	Lattice Parameter (Å)	Heat of Mixing (KJ/mol)	Cohesive Energy (eV/atom)	Deviation from Vegard's law (%)
(Fe-Ni)	3.538	0.176	-4.423	-0.07%
(Fe-Cr)	3.544	0.393	-4.296	-0.003%
(Fe-Co)	3.554	0.109	-4.404	-0.03%
(Cr-Co)	3.539	0.144	-4.303	-0.03%
(Ni-Cr)	3.524	0.095	-4.324	-0.02%
(Ni-Co)	3.535	0.135	-4.429	-0.01%
(Ni-Ti)	3.925	27.02	-4.372	8%
(Cr-Ti)	3.948	25.4	-4.262	9.8%
(Fe-Ti)	3.915	15.7	-4.462	5.0%
(Co-Ti)	3.970	25.9	-4.362	11.0%

Table 3
Properties of the binary B2 equiatomic ordered mixtures as given by the potentials used in this work.

B2 ordered phase	Lattice parameter (Å)	Cohesive Energy (eV)
(NiTi)	3.078	-4.497
(CrTi)	3.089	-4.360
(FeTi)	3.125	-4.587
(CoTi)	3.081	-4.611

constant. A Ni substrate was also used in previous studies of deposition of HEA films [34,43,44]. The substrate crystal orientation is chosen to minimize epitaxial growth. The substrate has a dimension of 70 × 70 × 32 Å placed in a simulation box with a length of 162 Å along the *z* direction. Periodic boundary conditions are applied for the *x* and *y* directions. The *z* direction is non-periodic, and atoms are eliminated if they cross the top *z* boundary. The substrate is divided into 3 regions, i.e., frozen, thermostat, and Newtonian, following previous PVD simulations [28]. The frozen region is defined as the downmost 2 atomic layers along the *z* direction, where all atomic positions are fixed during the whole simulation. The thermostat region is the middle region with a thickness of 14 Å, where the temperature is held at 300 K using a Langevin thermostat [45]. The Newtonian region is the substrate surface with a thickness of 11 Å, where atoms can move freely.

We choose two HEA families, $CoFeNiTi_x$ and $CrFeNiTi_x$, to investigate the microstructure formation in thin films. *x* is the molar ratio with values of 0, 0.16, 0.33, 0.53, 0.75 and 1, denoted by Ti_0, $Ti_{0.16}$, $Ti_{0.33}$, $Ti_{0.53}$, $Ti_{0.75}$, and Ti_1, respectively. Interatomic forces are calculated using an EAM potential as discussed in section 2.2. To ensure the accuracy of the PVD simulation, a dynamic time step with a maximum value of 1 fs is employed in order to limit atomic motion displacement to a maximum of 0.2 Å per timestep. Before starting the PVD process, all substrate atoms are set at the desired temperature. The system is thermalized for 200,000 steps until the Newtonian region reaches a stable temperature of 300 K. Then, a total of 24,000 atoms are deposited on the substrate in each simulation, where Ti content is varied by adjusting the number of Ti atoms deposited. Atoms are inserted at the top *z* position in the simulation box, randomly in the *xy* plane, with velocity along the *z* direction with an energy of 1 eV, to match the energy of sputtered atoms under low Ar pressure [46]. The deposition rate for each element is defined by its content in a specific composition, i.e., the higher the content, the higher the deposition rate. The fastest deposition rate is limited to 1 atom per 5,000-timesteps, which ensures that the system has sufficient time to dissipate the heat generated by the deposition process and prevents the deposited layer from overheating. For example, for a composition of $CoFeNiTi_{0.53}$, we deposit 6,400 Co, Fe, and Ni and 4,800 Ti atoms. Since Co, Fe and Ni have the same and highest content, the deposition rate for them is set at 1 atom per 5,000-time steps. Thus, the deposition simulation takes a total of 32-million-time steps where one Co, Fe, and Ni atoms are deposited every 5,000-time steps. At the same

time one Ti atom is deposited every 6,666-time steps. We also estimate the cooling rate during the MD simulations. Specifically, we deposit a single atom and monitor the local temperature of the substrate region where the atom deposits. This local region has a hemisphere shape with a radius of 10 Å containing 138 atoms, whose center is defined by the impact position of the deposited atom. The radius of the hemisphere region is chosen to be slightly lower than the thickness of Newtonian region, in order to exclude the thermostat region. The temperature evolution of the local region and the corresponding cooling rate calculated from the first order derivative of the temperature before and after the deposition process is provided in Fig. S1. The estimated local heating and cooling rates during MD simulations of PVD reach up to 10^{14} K/s. We also provide a movie showing the swift heat dissipation during the PVD simulations in the Supplementary Materials.

In order to help understand the deposition results, we evaluate energy versus volume relationships for the HEA families in the FCC, HCP, BCC, and amorphous phases. Different crystalline structures are created by randomly populating the lattice sites with different elements based on the target chemical composition. To generate an amorphous structure, we employ a melting-quenching procedure. We heat an initially crystalline system from 150 K to 3000 K in 80 ps and thermalize the melt at 3000 K for 30 ps. We then quench the sample to 50 K using a quenching rate of 10^{15} K/s and finally relax the amorphous sample at 50 K for 20 ps. After creating the required systems, a conjugate gradient energy minimization is performed for each crystalline and amorphous system to reach the lowest energy state, corresponding to the lowest energy in the energy versus volume curves. The conjugate gradient is performed on the atom coordinates and the volume of the simulation box. The final configuration is used to evaluate the energy versus energy relationships by adjusting the volume of the simulation box while keeping the relative atoms positions fixed.

In order to isolate the effects of compositional and size fluctuations, additional simulations are performed using an AA force field that eliminates the distinction between different elements, i.e., interactions between different atoms are averaged. Three compositions ($x = 0$, 0.33, and 1) are selected for each HEA family. We replace all the elements in the previous simulation process with averaged sized atoms. In order to maintain the same substrate structure and lattice constant as FCC Ni (100), an extra harmonic potential force is independently applied to all atoms in the thermostat and Newtonian regions, with a force constant of 1 eV/Å^2. The remaining simulation processes are the same as described above. Visualizations and data analysis are performed with OVITO [47].

3. Results

As a first step, we characterize the microstructures of the deposited CoFeNiTi$_x$ and CrFeNiTi$_x$ thin films. Each HEA family has six distinct compositions, i.e., Ti$_0$, Ti$_{0.16}$, Ti$_{0.33}$, Ti$_{0.53}$, Ti$_{0.75}$, and Ti$_1$. The SEM micrographs of the CoFeNiTi$_x$ samples and their corresponding normalized XRD patterns are shown in Fig. 2. As shown in Figs. 2(a), (b), and (c), the surface micrographs of the samples with a low Ti content ($x < 0.53$) display a nanocrystalline structure. The average crystallite sizes are measured as 22.22, 35.56, and 9.65 nm for the Ti$_0$, Ti$_{0.16}$, and Ti$_{0.33}$ samples, respectively (see Table SIII). However, a significant morphological change occurs when the Ti content is increased to $x = 0.53$ and higher values. All three high Ti content samples, i.e., Ti$_{0.53}$, Ti$_{0.75}$, and Ti$_1$, feature an amorphous microstructure containing very fine crystallites approximately ~1.1 nm in size, as shown in Figs. 2(d), (e), and (f). This microstructural change is also reflected in the XRD diffractograms. Samples with a Ti content lower than 0.53 exhibit an FCC crystalline phase, while other samples containing more Ti show an amorphous hump as noted in Fig. 2(g). One should note that for the Ti$_{0.33}$ sample, the XRD pattern display a distinct spike along with the amorphous hump, suggesting that this composition is at the threshold point for the FCC to amorphous transition. Therefore, an increased Ti content can disrupt the crystallization process of CoFeNiTi$_x$ HEA thin films.

A similar effect of Ti is also observed in the CrFeNiTi$_x$ samples. Fig. 3 shows the surface micrographs and diffractograms for CrFeNiTi$_x$ thin films with Ti molar ratio from 0 to 1. In this scenario, only the sample without any Ti displays a crystalline morphology as shown in Fig. 3(a), with a crystallite size of 34.34 nm. All the other samples show an amorphous phase with a crystallite size from 1.14 to 3.33 nm (see Table SIII). This is also revealed by the XRD patterns provided in Fig. 3 (g). An FCC structure is detected in the Ti$_0$ sample, while amorphous humps are displayed in all other compositions, suggesting that the microstructural change occurs due to the presence of Ti. Moreover, the amorphous peak for the Ti$_{0.16}$ sample is slightly narrower than the other amorphous samples, indicating that this composition could be still within the transition zone from crystalline to amorphous. These results imply a critical Ti content leading to the formation of an amorphous microstructure for both CoFeNiTi$_x$ and CrFeNiTi$_x$ HEA thin films. The critical molar value identified is ~0.53 for CoFeNiTi$_x$ and is ~0.16 for CrFeNiTi$_x$.

In order to understand the role of Ti on the microstructure formation of HEA thin films prepared by sputtering, we perform MD simulations of the deposition process using the same compositions as in the experiments. Illustrations of the microstructure generated during the

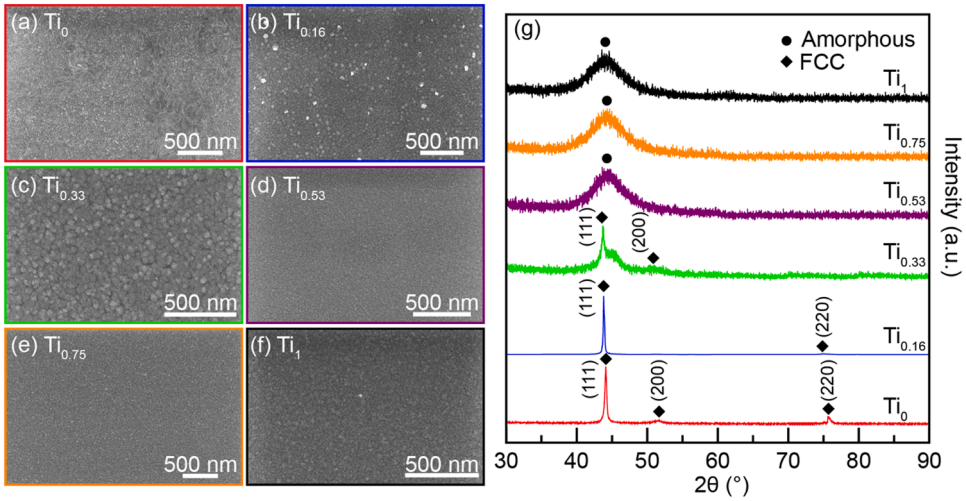

Fig. 2. Experimental surface SEM micrographs (a - f) for CoFeNiTi$_x$ sputtered thin films and their corresponding normalized X-ray diffractograms (g). SEM micrograph borders and diffractogram curves are color coded by Ti molar ratio.

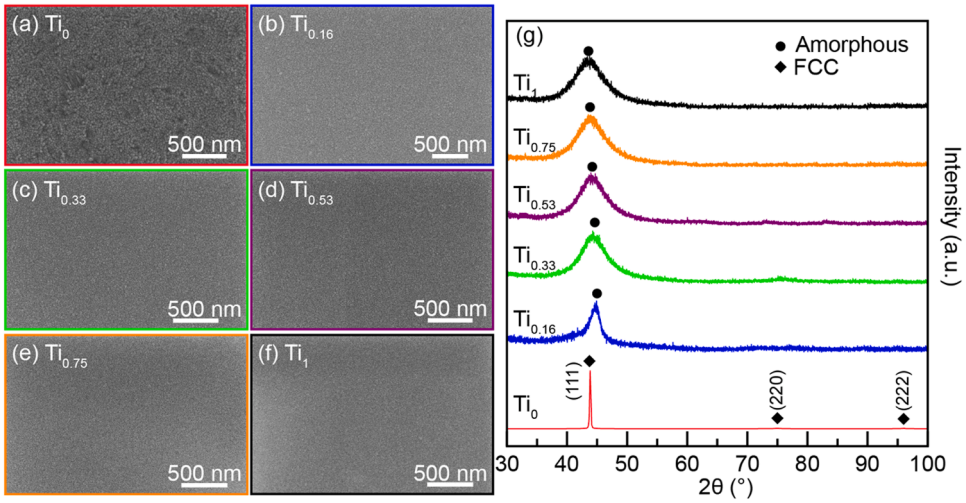

Fig. 3. Experimental surface SEM micrographs (a - f) for $CrFeNiTi_x$ sputtered thin films and their corresponding normalized X-ray diffractograms (g). SEM micrograph borders and diffractogram curves are color coded by Ti molar ratio.

deposition of $CoFeNiTi_x$ and $CrFeNiTi_x$ films are shown in Figs. 4 and 5, respectively. Different colors indicate different local structural environments, which are identified by the common neighbor analysis (CNA) algorithm [48]. The dashed lines indicate the separation between the deposited films and the defect free (100) FCC Ni substrates. One should note that while there are amorphous (labeled AM) and HCP local structural environments identified in the FCC solid solution films, they simply indicate the formation of local defects and not the presence of additional phases. The film surface is identified as amorphous due to the presence of the free surface. For the $CoFeNiTi_x$ HEA family, films with a Ti content below 0.53 favor an FCC structure, while other higher Ti content films form an amorphous structure, reproducing the trend and critical Ti content observed in the experimental $CoFeNiTi_x$ samples. The microstructures of $CrFeNiTi_x$ films shown in Fig. 5 show similar features as those of $CoFeNiTi_x$ films. However, the critical Ti content ~0.53 for $CrFeNiTi_x$ is higher than the value obtained from the experimentally produced films. Noteworthy, vacancies and point defects are detected in both $CoFeNiTi_x$ and $CrFeNiTi_x$ FCC films as indicated by a few local amorphous structures, which are generated during the film growth [49, 50]. Also, the $Ti_{0.16}$ and $Ti_{0.33}$ films for both $CoFeNiTi_x$ and $CrFeNiTi_x$ families show formation of stacking faults, denoted by the atoms in the HCP local structure, suggesting that the introduction of Ti lowers the stacking fault energy. The lower stacking fault energy can further lead to the formation of twin boundaries, which is commonly observed in the sputtering process of metallic systems [51,52]. For the amorphous films in both HEA families, the presence of a layer of FCC epitaxially grown structure can be observed. The thickness of the epitaxial layers decreases with the increase of Ti content, indicating that the addition of Ti contributes to the amorphization of HEA thin films.

To further compare the simulated grown film with the experimental samples, we generate simulated diffractograms. The XRD diffraction intensity is calculated for the simulated films using the model proposed by Coleman et al. [53]. Following the experimental diffractograms, we use an incident radiation wavelength of 1.5406 Å, and a 2θ range from 30° to 90° for the $CoFeNiTi_x$ films and from 30° to 100° for $CrFeNiTi_x$ films. To eliminate the effect of the substrate and the respective epitaxial growth in the very first layers of the film, we only select the top ~4.5 nm thick layer to do the calculations. The simulated XRD profiles are presented in Fig. 6, providing further evidence for the microstructure transition from FCC at low Ti content to amorphous at high Ti content. For both $CoFeNiTi_x$ and $CrFeNiTi_x$ HEA films, the critical Ti content is ~0.53. The positions of the peaks corresponding to FCC (111), (200), (220), and (222), are in good agreement with the experimental results. However, except the main (111) peak, other main peaks include several subsidiary peaks. Also, the intensities of the (200) peaks for Ti_0 and $Ti_{0.16}$ are much higher than expected compared to the (111) peak. These abnormal peaks may be a result of the finite size of the simulation cell [53].

It is worth quantifying the structure composition of different microstructures as a function of Ti content in the simulated HEA thin films. We calculate the structure composition of a given film by quantifying the fraction of total atoms in the system present in the different local structural environments using the CNA method. The results for $CoFeNiTi_x$ and $CrFeNiTi_x$ HEA thin films are shown in Fig. 7. For both alloy families, we can observe a smooth transition from an FCC dominated microstructure to a predominantly amorphous structure, with a

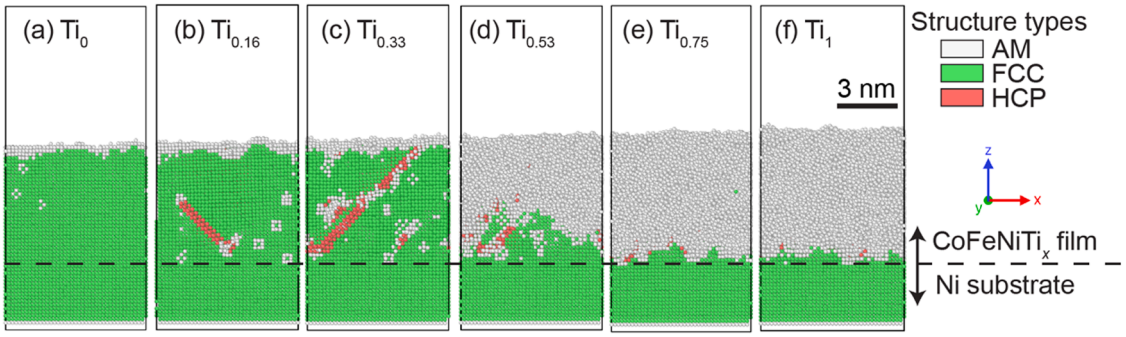

Fig. 4. $CoFeNiTi_x$ simulated thin film local structures for different Ti concentration from (a) $x = 0$ to (f) $x = 1$. The dashed line indicates the interface between the Ni substrate and the deposited film. The color of the atoms indicates the local structural environment, amorphous (AM), FCC, or HCP.

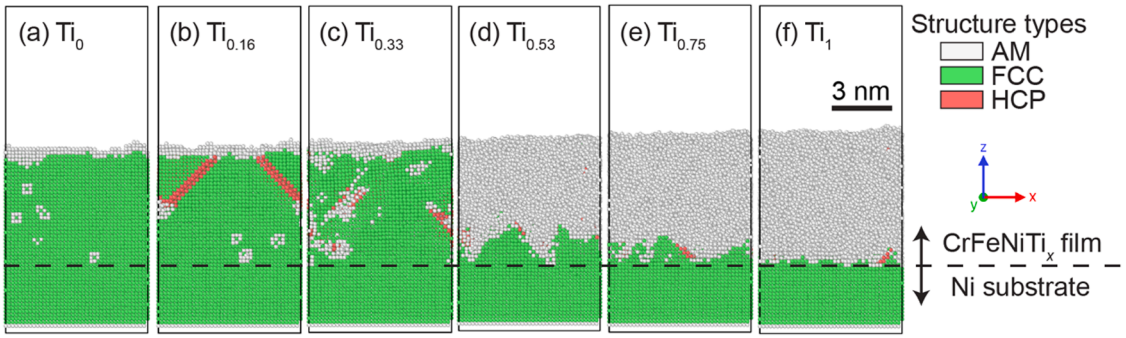

Fig. 5. CrFeNiTi$_x$ simulated thin film local structures for different Ti concentration from (a) $x = 0$ to (f) $x = 1$. The dashed line indicates the interface between the Ni substrate and the deposited film. The color of the atoms indicates the local structural environment, amorphous (AM), FCC, or HCP.

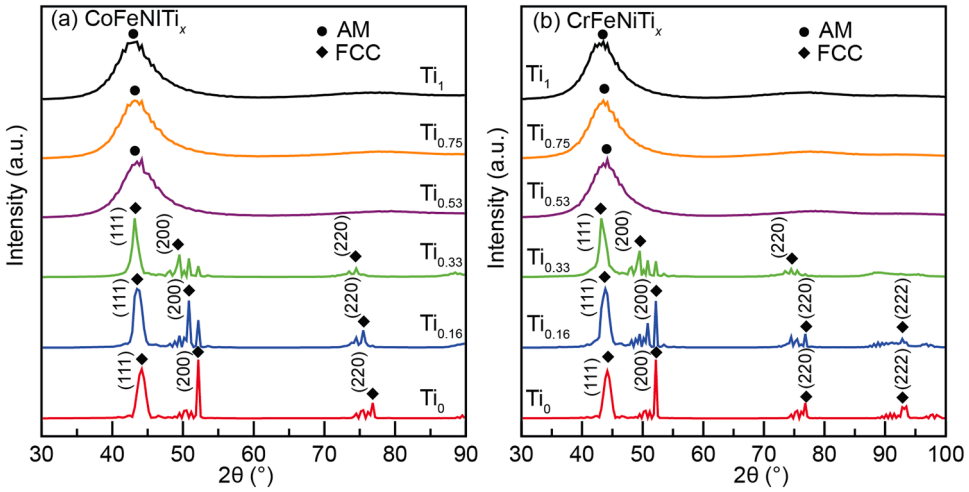

Fig. 6. Calculated X-ray diffractograms for (a) CoFeNiTi$_x$ and (b) CrFeNiTi$_x$ simulated thin films.

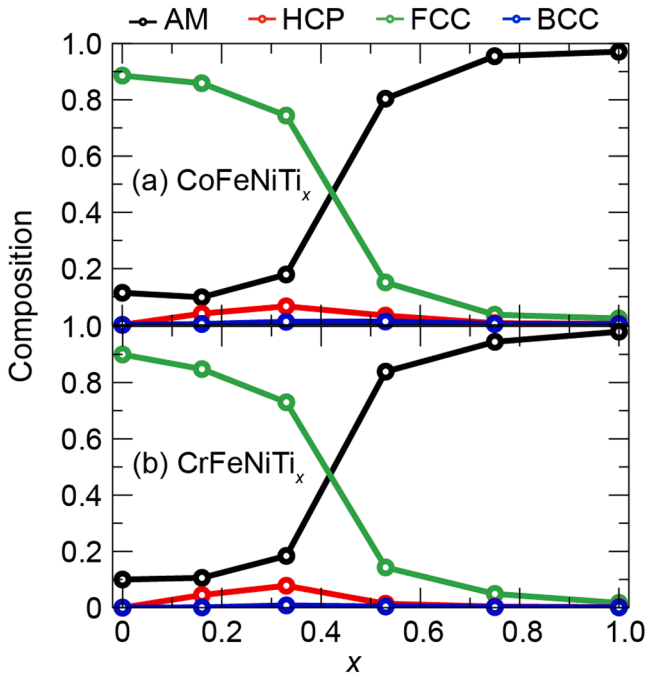

Fig. 7. Fraction of crystal and amorphous local structures as a function of Ti concentration in (a) CoFeNiTi$_x$ and (b) CrFeNiTi$_x$ simulated thin films.

threshold between $x = 0.33$ and 0.53. A small amount of HCP local structure is formed in low Ti content films with a maximum content at $x = 0.33$, indicating the formation of stacking faults, as observed in Figs. 4 and 5. This further demonstrates that the presence of Ti can reduce the stacking fault energy of CoFeNiTi$_x$ and CrFeNiTi$_x$ HEA thin films before favoring the formation of an amorphous structure. The results indicate the absence of BCC phase in all films simulated.

To further understand the crystalline and amorphous phase stability of the HEA films, we calculate the energy versus volume relationships for FCC, HCP, BCC, and amorphous structures. The results for CoFeNiTi$_x$ alloys are shown in Fig. 8. As seen in Fig. 8(a), the order of the phase stability is FCC, HCP, BCC, and amorphous in the absence of Ti. This stability order is preserved as the Ti content is raised to 0.53, yet the energy differences between competing phases decrease substantially, suggesting that the FCC and HCP phase stabilities are reduced with the introduction of Ti. At high Ti content, Ti$_{0.75}$ and Ti$_1$, the BCC becomes the most stable phase, while the FCC, HCP, and amorphous curves largely overlap indicating similar stability. However, in both the experimental and simulated CoFeNiTi$_x$ thin films, we observe an FCC to amorphous transition instead of FCC to BCC, contrasting the phase energetics results. This may be due to the fast-cooling rate inherent to the PVD process, suppressing atomic diffusion and phase formation. Also, even though the BCC structure is preferred in Ti$_{0.75}$ and Ti$_1$ as shown in Figs. 8(e) and (f), the energy differences between BCC and other structures are not significant. As a result, there is no strong driving force at those chemical compositions to form the lowest energy BCC phase.

The energy vs volume results for the CrFeNiTi$_x$ HEA family are shown in Fig. 9. We find a similar trend as observed for the CoFeNiTi$_x$, i.e., the addition of Ti reduces the stability of the FCC and HCP phases and

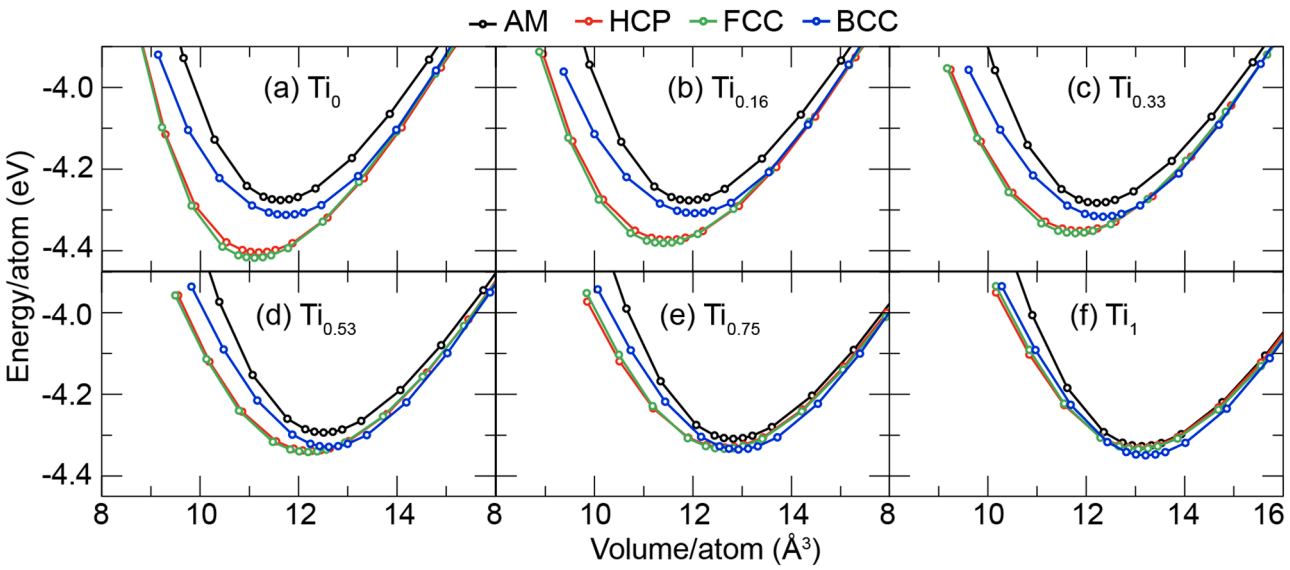

Fig. 8. Energy vs volume relationships for AM, HCP, FCC, and BCC phases of $CoFeNiTi_x$ alloys. (a) - (f) Ti molar ratio varies from 0 to 1.

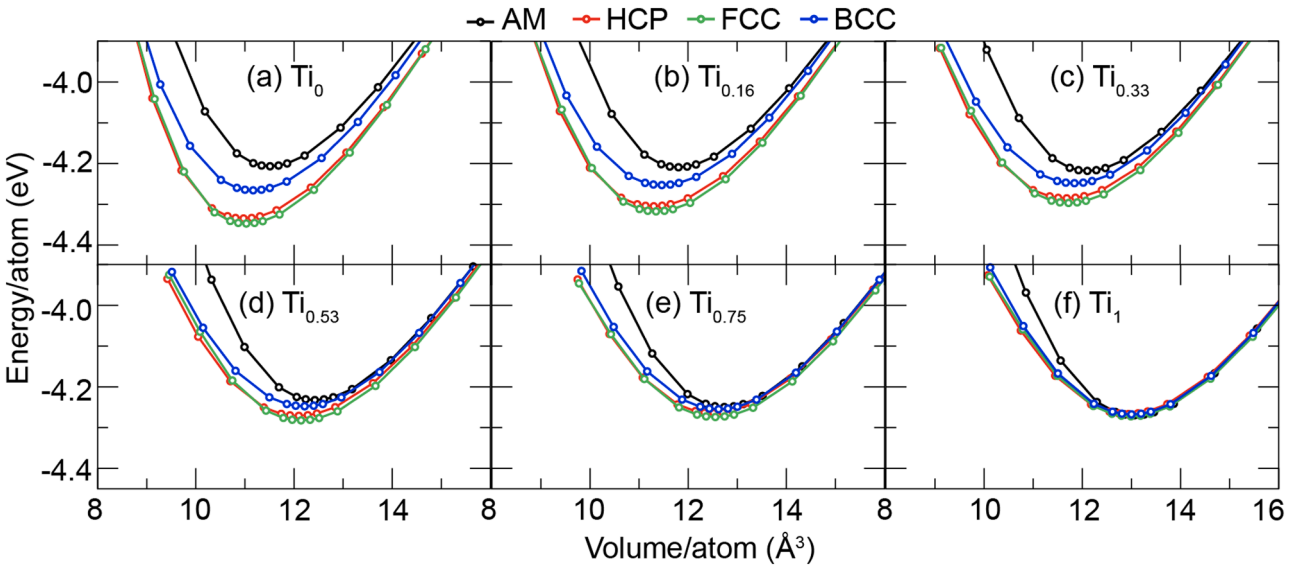

Fig. 9. Energy vs volume relationships for AM, HCP, FCC, and BCC phases of $CrFeNiTi_x$ alloys. (a) - (f) Ti molar ratio varies from 0 to 1.

overall reduces the energy difference between different phases. Nevertheless, the FCC is the most favorable phase, except for the equiatomic composition case, when $x = 1$. Here, energy curves largely overlap, implying the stability of the amorphous phase, due to the lack of driving force for crystal formation. The microstructures of the experimental and simulated $CrFeNiTi_x$ thin films slightly deviate from the predictions of energy vs volume calculations by showing a lower Ti content threshold for the transition from crystalline to amorphous phase stability. In experimental samples the transition occurs at $x = 0.16$ while in simulations the calculated value is $x = 0.53$. This can be explained by the suppression of atomic diffusion during the fast PVD process as well as the low driving force to form a crystalline phase at high Ti content. Moreover, for both CoFeNiTi and CrFeNiTi systems shown in Figs. 8 and 9, the energy minimum for each system shifts from ~11 to ~13 $Å^3$/atom, as the Ti content increases. The shift indicates that the extra volume introduced by the disorder in the amorphous phase is offset at high Ti content by the large atomic size differences between Ti and other elements in the alloy, resulting in an energy minimum at ~13 $Å^3$/atom for all phases considered.

In order to further understand the effect of atomic size difference in the phase stability of the HEA thin films, we perform an additional set of PVD simulations using an AA potential. We consider three compositions in each alloy family, i.e., Ti_0, $Ti_{0.33}$, and Ti_1. We also calculate the energy versus volume relationship for each system at each composition. The results for $CoFeNiTi_x$ HEAs are shown in Fig. 10. For Ti_0 and $Ti_{0.33}$, both the energy profiles and microstructures are comparable to the previous experimental and simulated results, i.e., low Ti content samples favor the FCC phase. In contrast, the Ti_1 thin film shown in the right panel of Fig. 10(c) displays a BCC phase. That agrees with the energy versus volume curves shown in Fig. 10(c), which shows the stability of the BCC phase. To be noted, grain boundaries are formed during the growth of the BCC film, which is indicated by the atoms colored in gray (amorphous structure) that are also found at the surface and in the interface between the film and substrate phases. This result contrasts with the formation of the amorphous structure discussed above and suggests that the amorphous phase stability in high Ti content HEA thin films is caused directly by the large atomic size difference. We can draw similar conclusions from the results shown in Fig. 11 for the $CrFeNiTi_x$. An FCC

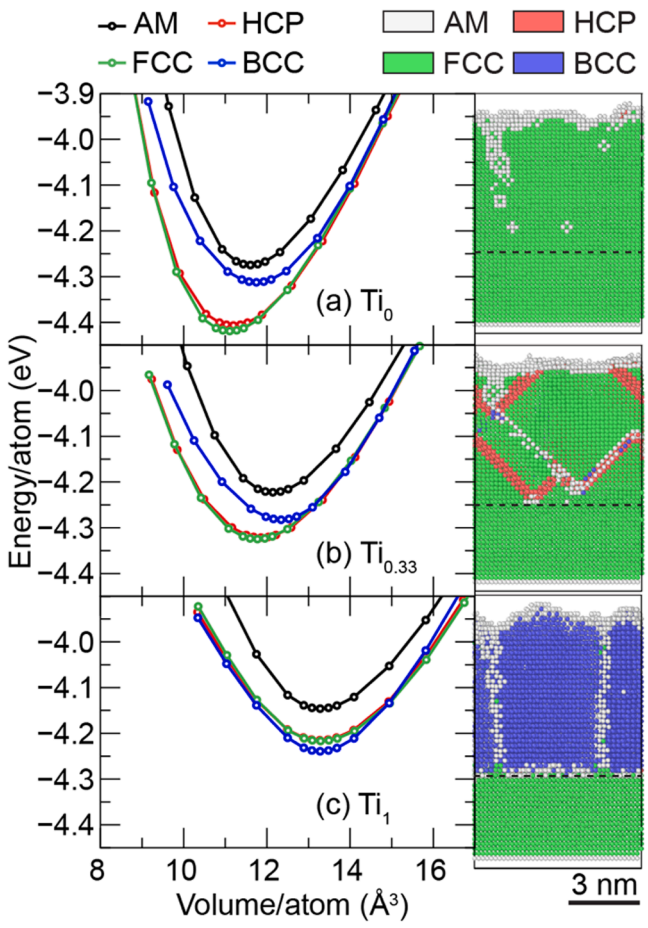

Fig. 10. Energy versus volume relationships and corresponding thin films of $CoFeNiTi_x$ alloys using the average-atom potential. (a) $x = 0$, (b) $x = 0.33$, and (c) $x = 1$. The black dashed line indicates the interface between the substrate and deposited film.

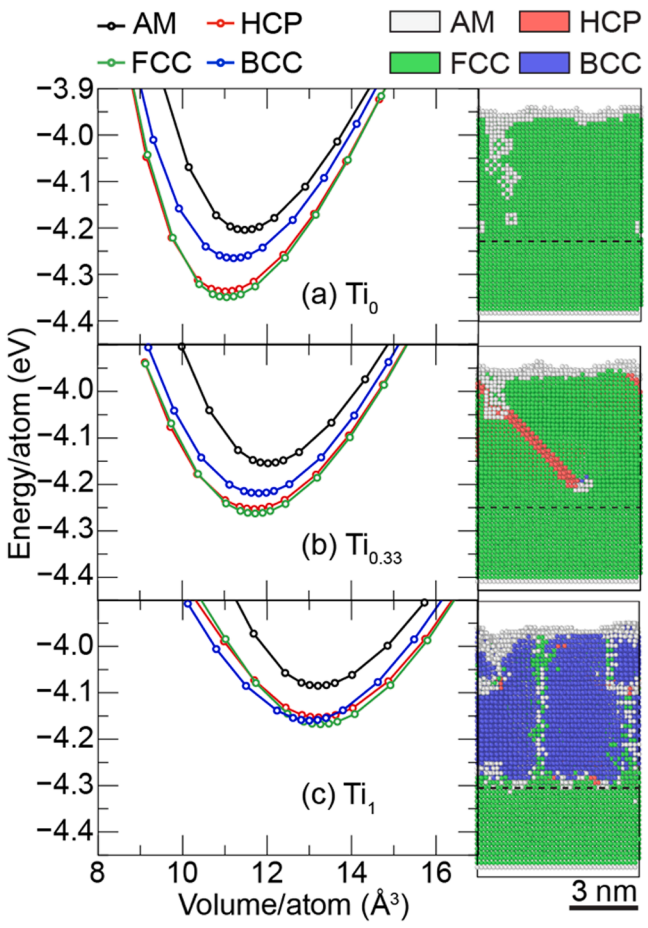

Fig. 11. Energy versus volume relationships and corresponding thin films of $CrFeNiTi_x$ alloys using the average-atom potential. (a) $x = 0$, (b) $x = 0.33$, and (c) $x = 1$. The black dashed line indicates the interface between the substrate and deposited film.

to BCC phase stability crossover is observed when the atomic size difference between different elements is eliminated. As mentioned in the Methodology section, an extra harmonic force is applied to the substrate atoms in order to preserve the lattice constant of Ni. The relaxed FCC lattice formed by the averaged atoms for $Ti_{0.33}$ and Ti_1 would have a larger lattice constant than Ni, as the energy minimum shifts to larger volumes with Ti molar fraction increase, as shown in Figs. 10 and 11. Thus, even though the FCC phase has the lowest energy for $CrFeNiTi_1$ shown in the energy profiles in Fig. 11(c), the film still forms a BCC phase because the volume per atom is smaller than the most relaxed state, where BCC is the most stable phase. These results provide direct insights into the relationship between the atomic size difference and the phase stability of HEA thin films.

4. Discussion

The results presented in this work help to understand the effect of Ti content on the microstructure formation of $CoFeNiTi_x$ and $CrFeNiTi_x$ thin films. As shown in Figs. 2, 3, 4, and 5, both experimental and modeling results highlight a phase transition from FCC to amorphous structure for increasing Ti content in the HEA films. The threshold Ti content is identified as ~0.53 and ~0.16 in experiments, and ~0.53 and ~0.53 in simulations for $CoFeNiTi_x$ and $CrFeNiTi_x$, respectively.

For additional clarity, we undertook molecular statics simulations to examine the inherent thermodynamic stability of the various phases, which is independent of the cooling rate. These simulations, conducted for both the alloy and the average-atom material, further corroborate that size differences indeed facilitate the stabilization of the amorphous phase in such compositionally complex materials, irrespective of the cooling rate. The outcomes of this thermodynamic phase stability analysis are reported in Figs. 8 through 11. Notably, these results exclude any consideration of the cooling rate, as they represent equilibrium calculations.

Our observation of the transition in phase stability reported in Figs. 8 and 9 are in good agreement with previous studies. For example, Hsu et al. [23] synthesized $CoCrFeMnNiTi_x$ HEA films by magnetron sputtering and found that the film favors an amorphous structure when the Ti content is higher than 0.4. In another investigation on the microstructure formation in $AlCrFeNiTi_x$ and $AlCoFeNiTi_x$ HEA films, Goodelman et al. [18] showed that both compositions displayed an amorphous structure at high Ti content. In order to understand such effects, we perform additional MD simulations on the $CoFeNiTi_x$ and $CrFeNiTi_x$ HEA systems yet using the AA force field, which eliminates the atomic size difference among different constituent elements. Results shown in Figs. 10 and 11 demonstrate that the microstructures for all compositions display a crystalline structure, suggesting that the large atomic size difference between the large Ti and other small elements directly causes the amorphization in $CoFeNiTi_x$ and $CrFeNiTi_x$ films. By comparing the energy profiles calculated from the AA potential, one can note that the amorphous phase is always the least stable phase. Also, the amorphous phase preserves a relatively large energy difference with other crystalline phases even though the Ti content is $x = 1$, in contrast to what we have seen in the energy profiles calculated from the EAM potential. Therefore, the large atomic size difference is a key factor that

influences the microstructure formation in the HEA films, i.e., a large atomic size difference significantly enhances the energy stability for the amorphous phase in comparison with the counterpart crystalline phases [54].

Atomic size difference is also an important parameter that was used in empirical models to predict SS, intermetallic, and amorphous phases in HEAs [26,55–57]. Hence, it is worth quantifying the atomic size differences for compositions employed in this work and comparing them with existing predictive models. Yang and Zhang [55] proposed two parameters based on as-cast HEA samples, Ω and δr, that can be used as criteria to predict the phase formation for a given HEA composition. Ω describes the competition between entropy of mixing, ΔS_{mix}, and enthalpy of mixing, ΔH_{mix}, while δr quantifies the atomic radius difference between component elements. The empirical SS formation range is located at $\Omega \geq 1.1$ and $\delta r \leq 6.6\%$. The formulas for Ω, δr, ΔS_{mix} and ΔH_{mix} are shown in Eqs. 1-4.

$$\Omega = \left(\sum_{i=1}^{n} c_i T_{m,i}\right) \Delta S_{mix} \Big/ |\Delta H_{mix}| \tag{1}$$

$$\delta r = \sqrt{\sum_{i=1}^{n} c_i \left(1 - \frac{r_i}{\bar{r}}\right)^2} \tag{2}$$

$$\Delta S_{mix} = -R \sum_{i=1}^{n} c_i \ln(c_i) \tag{3}$$

$$\Delta H_{mix} = \sum_{i<j}^{n} 4 H_{ij} c_i c_j \tag{4}$$

where c_i, $T_{m,i}$, and r_i are the atomic fraction, melting temperature, and atomic radius of the ith element in an HEA that contains n elements, $R = 8.314$ $JK^{-1}mol^{-1}$ is the gas constant, H_{ij} is the enthalpy of mixing of element i and j at the equimolar concentration in regular binary solutions [58], and $\bar{r}$ is the average atomic radius given by $\bar{r} = \sum_i^n c_i r_i$. Here, we calculate Ω and δr for all the compositions studied in this work. The results are summarized in Fig. 12, which shows that increasing Ti content in both HEA families leads to a smaller Ω yet a larger δr. This indicates that samples with a high Ti content have less tendency to form a SS phase, supporting the phase transition observed in both experiments and MD simulations. However, the Ω and δr SS formation thresholds identified here are different from those mentioned in the above model. Based on the simulation results, the range for FCC formation is $\Omega \geq 1.7$ and $\delta r \leq 5.7$ % for both $CoFeNiTi_x$ and $CrFeNiTi_x$. In addition, from the experimental results, we cannot identify a single threshold for these two HEA families. These deviations may be due to the non-equilibrium state of HEA thin films prepared by PVD since the model is proposed mostly for casting sample microstructures [3]. Thus, these two parameters, Ω and δr, provide a reasonable estimate for the phase formation in HEAs, yet the SS formation threshold values depend on the synthesis method and the specific HEA system.

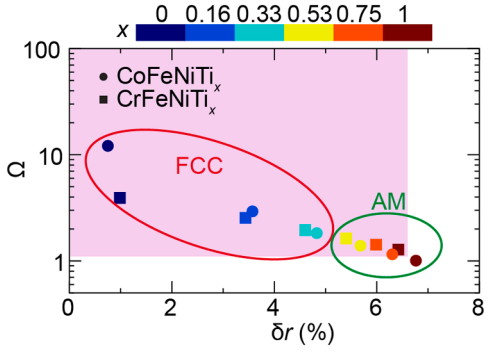

Fig. 12. Ω and δr relationships for $CoFeNiTi_x$ and $CrFeNiTi_x$ alloys. Colors represent the Ti contents from 0 to 1. The purple region highlights the solid solution formation range, $\Omega \geq 1.1$ and $\delta r \leq 6.6\%$. The red and green circles group the compositions that form FCC and AM phases in the simulated films, respectively.

Similar to Ti, Al is another common alloy element that has a relatively large atomic radius (> 1.4 Å) and its effect on the microstructure formation of HEA films has been investigated in several studies [12,18,59]. Even though Al introduces a comparable atomic size difference as Ti, it has been reported that Al has a different impact on the phase formation. For example, Kube et al. [12] synthesized a large amount of HEA films and found that the increasing atomic size difference introduced by Al led to an FCC to BCC phase transition. Arguably, the BCC preference for high Al content samples stems from the loosely packed nature of BCC structure that can accommodate the lattice distortion and strain caused by a large atomic size difference. This contrasts to the FCC to amorphous phase transition observed at different Ti contents. One possible reason for the distinct effect of Al is that Al prefers to form a strong electronic interaction with other transition metals because of its high electron density and Fermi level [60]. Moreover, Al has a lower $|\Delta H_{mix}|$ than Ti when mixing with other small elements based on the H_{ij} obtained in Ref. [58]. The calculated Ω increases if replacing the Ti with the same amount of Al in a certain composition. Also, the δr decreases due to the slightly lower atomic radius of Al than Ti. Thus, HEA systems with the presence of Al have a greater tendency to form a SS phase than Ti, suggesting that the phase formation in HEA films is controlled by the atomic radius difference δr as well as the chemistry of the specific atomic species. Furthermore, as shown in Figs. 8 and 9, the energy for BCC structures drops with the increasing Ti content in both HEA families, indicating that the BCC phase is more stable at high Ti content, i.e., large atomic size difference. However, the amorphous phase also becomes stable and the energy difference between crystalline and amorphous phases is no longer significant, leading to the amorphous phase in high Ti content samples.

After having discussed the effect of atomic size difference, it is instructive to discuss the effect of high cooling rate inherent to PVD. Although there is very limited data available for the microstructures of as-casted samples that have the same compositions as this work, literature reports have shown that the addition of Ti significantly affects the stability of the FCC crystal structure in the as-cast samples [24,61,62,9,63]. These reports suggest that the addition of Ti may lead to the formation of a complex microstructure combining multiple intermetallic compounds and different phases. However, studies on HEA thin films prepared by sputtering have found that the high cooling rate (10^9 - 10^{11} K/s) can limit atomic diffusion and kinetically suppress the formation of such phases, thus favoring the formation of a single SS or amorphous phase during the sputtering process [12,13,18,19,64–66]. For example, Kube et al. [12] compared the phase formation in as-sputtered and as-casted samples with the same composition and found that only a single SS phase formed for all as-sputtered samples. In this study, we also observe that only a single phase is formed in all the samples prepared by experiments, i.e., either FCC or amorphous, which is expected for PVD. In MD simulations, the estimated cooling rate (~10^{14}) is even higher than that in sputtering as shown in Fig S1. Even though the cooling rate in MD simulations is several orders of magnitude larger than that in sputtering experiments, remarkably, we still observe the same FCC to amorphous phase transition from a low to high Ti content in both HEA families in the simulation results. The MD simulations employed in this work are designed to scrutinize why particular phases are energetically preferred and tend to form during the sputtering process, which presumes a high cooling rate. Hence, the simulations enable us to pinpoint the impact of atomic size discrepancy on phase formation in sputtered HEAs. Due to the limited time scale of MD simulations, it is often challenging to observe the formation of intermetallic phases. For the same reasons, MD simulations of PVD are suitable for reproducing the experimental sputtering process and predicting the kinetically or energetically favorable phases in HEA thin films.

We note that when using empirical interatomic potentials, agreement with experiments is generally "semi-quantitative", meaning empirical potentials can reliably be used to study trends but should not be expected to have quantitative predictive capabilities. This is particularly true for multi-component complex systems, such as the one used here. In particular, the set of potentials used in the present work is not developed to reproduce any possible ordering effects. The difference in the critical Ti content required for amorphous phase formation in the two HEA systems may be related to short range ordering, that is not included in the development of the empirical interatomic potential model. Specific thresholds for the crystal to amorphous transition will require further refinement of the EAM models utilized in this work.

Another factor that may affect the phase formation is the substrate used in the PVD process. It is known that the substrate composition, temperature, and lattice orientation could influence the microstructure formation and properties of thin films synthesized by sputtering [34, 67–70]. In the simulations, we are using a (100) FCC Ni substrate due to the lack of suitable interatomic potentials between Si and the metallic systems here. Thus, epitaxial growth is possible and expected in MD simulations. Nevertheless, not all films can grow epitaxially and form a single FCC structure. We observe defects, stacking faults, as well as amorphous phase, even though there are several epitaxial layers as shown in Figs. 4 and 5, suggesting that the effect of the substrate is negligible. For samples simulated using the AA potential, we use a substrate composed of AA atoms with the same lattice constant as Ni to maintain the same substrate size for consistency with the previous simulations. That leads to a smaller volume per atom in the film such that a BCC structure is formed for both $CoFeNiTi_1$ and $CrFeNiTi_1$. Although the substrate may influence which SS phase forms, we can still see the decreased amorphous phase stability and the formation of a SS phase after eliminating the atomic size difference among all the elements.

5. Conclusion

In summary, we use magnetron sputtering and MD simulations to investigate microstructure formation in $CoFeNiTi_x$ and $CrFeNiTi_x$ HEA thin films. Six distinct compositions were used for each HEA family to clarify the effect of atomic size difference on phase formation. Results showed that both $CoFeNiTi_x$ and $CrFeNiTi_x$ HEA films displayed a transition in phase stability from FCC to amorphous phase with increasing Ti content, in excellent agreement with previous studies. The threshold Ti content was identified as ~0.53 and ~0.16 for the $CoFeNiTi_x$ and $CrFeNiTi_x$ films prepared by sputtering, and ~0.53 and ~0.53 for samples prepared by MD simulations. The MD simulations reproduce the experimental results rather well despite the "model" nature of the interatomic potential. This is because the potentials do capture the size differences which are critical for the phase formation. Energy versus volume relationships suggested that the increasing Ti content stabilized the amorphous phases and reduced the driving force to form a crystalline structure. To further demonstrate the effect of large atomic size difference introduced by Ti, we performed additional MD simulations using an AA potential. In contrast to the previous results, samples with a high Ti content formed single crystalline structures. With the elimination of the atomic size difference among different elements, the energetic stability of the amorphous phase vanished. The formation of an amorphous phase in HEA thin films generated by PVD is therefore directly due to the atomic size difference. This work highlights the role of large atomic size difference in HEAs and provides guidance for future alloy design and applications. This work also demonstrates that MD simulations can be used as an efficient predictive tool to explore and screen the enormous HEA composition space.

Declaration of Competing Interest

The authors declare that they have no known competing financial interests or personal relationships that could have appeared to influence the work reported in this paper.

Acknowledgements

This material is based upon work supported by the National Science Foundation (Grant Number OISE-2106597). We acknowledge the Center for Advanced Research Computing (CARC) at the University of Southern California for providing computing resources that have contributed to the research results reported within this publication. URL: https://carc.usc.edu. We further acknowledge the Core Center for Excellence in Nano Imaging at USC for the use of their electron microscopy tools and XRD.

Supplementary materials

Supplementary material associated with this article can be found, in the online version, at doi:10.1016/j.actamat.2023.119163.

References

[1] B. Cantor, I.T.H. Chang, P. Knight, A.J.B. Vincent, Microstructural development in equiatomic multicomponent alloys, Materials Science and Engineering A 375 (2004) 213–218, https://doi.org/10.1016/j.msea.2003.10.257.
[2] J.W. Yeh, S.K. Chen, S.J. Lin, J.Y. Gan, T.S. Chin, T.T. Shun, C.H. Tsau, S.Y. Chang, Nanostructured high-entropy alloys with multiple principal elements: Novel alloy design concepts and outcomes, Adv Eng Mater 6 (2004) 299–303, https://doi.org/10.1002/adem.200300567.
[3] D.B. Miracle, O.N. Senkov, A critical review of high entropy alloys and related concepts, Acta Mater 122 (2017) 448–511, https://doi.org/10.1016/j.actamat.2016.08.081.
[4] S. Ranganathan, Alloyed pleasures: Multimetallic cocktails, Curr Sci 85 (2003) 1404–1406.
[5] M.H. Tsai, J.W. Yeh, High-entropy alloys: A critical review, Mater Res Lett 2 (2014) 107–123, https://doi.org/10.1080/21663831.2014.912690.
[6] Y. Zhang, T.T. Zuo, Z. Tang, M.C. Gao, K.A. Dahmen, P.K. Liaw, Z.P. Lu, Microstructures and properties of high-entropy alloys, Prog Mater Sci 61 (2014) 1–93, https://doi.org/10.1016/j.pmatsci.2013.10.001.
[7] B. Gludovatz, A. Hohenwarter, D. Catoor, E.H. Chang, E.P. George, R.O. Ritchie, A fracture-resistant high-entropy alloy for cryogenic applications, Science 345 (2014) (1979) 1153–1158, https://doi.org/10.1126/science.1254581.
[8] Y.F. Kao, S.K. Chen, T.J. Chen, P.C. Chu, J.W. Yeh, S.J. Lin, Electrical, magnetic, and Hall properties of AlxCoCrFeNi high-entropy alloys, J Alloys Compd 509 (2011) 1607–1614, https://doi.org/10.1016/J.JALLCOM.2010.10.210.
[9] Y. Li, Y. Miao, J. Feng, X. Wu, L. Pang, S. Gao, Y. Sui, J. QI, F. Wei, Q. Meng, Z. Zhan, Y. Ren, P. Cao, Z. Sun, L. Zhang, Electrothermal, magnetic properties and microstructure of CrFeNiTi x compositionally complex alloys, Ferroelectrics 584 (2021) 100–112, https://doi.org/10.1080/00150193.2021.1984771.
[10] D.B. Miracle, High entropy alloys as a bold step forward in alloy development, Nat Commun 10 (2019) 1–3, https://doi.org/10.1038/s41467-019-09700-1.
[11] D. Miracle, B. Majumdar, K. Wertz, S. Gorsse, New strategies and tests to accelerate discovery and development of multi-principal element structural alloys, Scr Mater 127 (2017) 195–200, https://doi.org/10.1016/J.SCRIPTAMAT.2016.08.001.
[12] S.A. Kube, S. Sohn, D. Uhl, A. Datye, A. Mehta, J. Schroers, Phase selection motifs in High Entropy Alloys revealed through combinatorial methods: Large atomic size difference favors BCC over FCC, Acta Mater 166 (2019) 677–686, https://doi.org/10.1016/j.actamat.2019.01.023.
[13] W. Li, P. Liu, P.K. Liaw, Microstructures and properties of high-entropy alloy films and coatings: A review, Mater Res Lett 6 (2018) 199–229, https://doi.org/10.1080/21663831.2018.1434248.
[14] W. Liao, S. Lan, L. Gao, H. Zhang, S. Xu, J. Song, X. Wang, Y. Lu, Nanocrystalline high-entropy alloy (CoCrFeNiAl0.3) thin-film coating by magnetron sputtering, Thin Solid Films 638 (2017) 383–388, https://doi.org/10.1016/J.TSF.2017.08.006.
[15] S. Fang, C. Wang, C.L. Li, J.H. Luan, Z.B. Jiao, C.T. Liu, C.H. Hsueh, Microstructures and mechanical properties of CoCrFeMnNiVx high entropy alloy films, J Alloys Compd 820 (2020), 153388, https://doi.org/10.1016/J.JALLCOM.2019.153388.
[16] Y.S. Kim, H.J. Park, S.C. Mun, E. Jumaev, S.H. Hong, G. Song, J.T. Kim, Y.K. Park, K.S. Kim, S. Jeong, Y.H. Kwon, K.B. Kim, Investigation of structure and mechanical properties of TiZrHfNiCuCo high entropy alloy thin films synthesized by magnetron sputtering, J Alloys Compd 797 (2019) 834–841, https://doi.org/10.1016/J.JALLCOM.2019.05.043.
[17] B.R. Braeckman, D. Depla, Structure formation and properties of sputter deposited Nbx-CoCrCuFeNi high entropy alloy thin films, J Alloys Compd 646 (2015) 810–815, https://doi.org/10.1016/J.JALLCOM.2015.06.097.
[18] D.C. Goodelman, D.E. White, A.M. Hodge, Phase transition zones in compositionally complex alloy films influenced by varying Al and Ti content, Surf Coat Technol 424 (2021), 127651, https://doi.org/10.1016/j.surfcoat.2021.127651.

[19] L. Zendejas Medina, L. Riekehr, U. Jansson, Phase formation in magnetron sputtered CrMnFeCoNi high entropy alloy, Surf Coat Technol 403 (2020), 126323, https://doi.org/10.1016/j.surfcoat.2020.126323.
[20] X. Wang, H. Xie, L. Jia, Z. Lu, Effect of Ti, Al and Cu addition on structural evolution and phase constitution of FeCoNi system equimolar alloys, Materials Science Forum 724 (2012) 335–338, https://doi.org/10.4028/www.scientific.net/MSF.724.335.
[21] J. Ding, H. Xu, X. Li, M. Liu, T. Zhang, The similarity of elements in multi-principle element alloys based on a new criterion for phase constitution, Mater Des 207 (2021), 109849, https://doi.org/10.1016/j.matdes.2021.109849.
[22] X. Wang, Q. Liu, Y. Huang, L. Xie, Q. Xu, T. Zhao, Effect of Ti content on the microstructure and corrosion resistance of CoCrFeNiTix high entropy alloys prepared by laser cladding, Materials 13 (2020) 2209, https://doi.org/10.3390/ma13102209.
[23] Y.C. Hsu, C.L. Li, C.H. Hsueh, Modifications of microstructures and mechanical properties of CoCrFeMnNi high entropy alloy films by adding Ti element, Surf Coat Technol 399 (2020), 126149, https://doi.org/10.1016/J.SURFCOAT.2020.126149.
[24] K.B. Zhang, Z.Y. Fu, J.Y. Zhang, W.M. Wang, H. Wang, Y.C. Wang, Q.J. Zhang, J. Shi, Microstructure and mechanical properties of CoCrFeNiTiAlx high-entropy alloys, Materials Science and Engineering A 508 (2009) 214–219, https://doi.org/10.1016/j.msea.2008.12.053.
[25] C.C. Tung, J.W. Yeh, T.T. Shun, S.K. Chen, Y.S. Huang, H.C. Chen, On the elemental effect of AlCoCrCuFeNi high-entropy alloy system, Mater Lett 61 (2007) 1–5, https://doi.org/10.1016/J.MATLET.2006.03.140.
[26] Y. Zhang, Y.J. Zhou, J.P. Lin, G.L. Chen, P.K. Liaw, Solid-Solution Phase Formation Rules for Multi-component Alloys, Adv Eng Mater 10 (2008) 534–538, https://doi.org/10.1002/ADEM.200700240.
[27] Y. Zhang, X. Yang, P.K. Liaw, Alloy design and properties optimization of high-entropy alloys, JOM 64 (2012) 830–838, https://doi.org/10.1007/s11837-012-0366-5.
[28] M.G. Eberhardt, A.M. Hodge, P.S. Branicio, Atomistic modeling of physical vapor deposition on complex topology substrates, Comput Mater Sci 203 (2022), 111111, https://doi.org/10.1016/j.commatsci.2021.111111.
[29] J. Wang, H. Huang, S.V. Kesapragada, D. Gall, Growth of Y-shaped nanorods through physical vapor deposition, Nano Lett 5 (2005) 2505–2508, https://doi.org/10.1021/nl0518425.
[30] S. Inoue, Y. Matsumura, Molecular dynamics simulation of physical vapor deposition of metals onto a vertically aligned single-walled carbon nanotube surface, Carbon N Y 46 (2008) 2046–2052, https://doi.org/10.1016/J.CARBON.2008.08.017.
[31] G.B. Bokas, L. Zhao, D. Morgan, I. Szlufarska, Increased stability of CuZrAl metallic glasses prepared by physical vapor deposition, J Alloys Compd 728 (2017) 1110–1115, https://doi.org/10.1016/J.JALLCOM.2017.09.068.
[32] L. Xie, P. Brault, A.L. Thomann, X. Yang, Y. Zhang, G. Shang, Molecular dynamics simulation of Al-Co-Cr-Cu-Fe-Ni high entropy alloy thin film growth, Intermetallics (Barking) 68 (2016) 78–86, https://doi.org/10.1016/j.intermet.2015.09.008.
[33] W.M. Choi, Y.H. Jo, S.S. Sohn, S. Lee, B.J. Lee, Understanding the physical metallurgy of the CoCrFeMnNi high-entropy alloy: An atomistic simulation study, NPJ Comput Mater 4 (2018) 1–9, https://doi.org/10.1038/s41524-017-0060-9.
[34] V.T. Nguyen, V.T.T. Nhu, X.T. Vo, Deposition characteristics of CoCrFeMnNi high-entropy alloys thin film via simulation, J Cryst Growth 603 (2022), 127004, https://doi.org/10.1016/J.JCRYSGRO.2022.127004.
[35] D. Farkas, A. Caro, Model interatomic potentials for Fe-Ni-Cr-Co-Al high-entropy alloys, J Mater Res 35 (2020) 3031–3040, https://doi.org/10.1557/jmr.2020.294.
[36] C.J. Ruestes, D. Farkas, Dislocation emission and propagation under a nano-indenter in a model high entropy alloy, Comput Mater Sci 205 (2022), 111218, https://doi.org/10.1016/j.commatsci.2022.111218.
[37] M.S. Daw, M.I. Baskes, Embedded-atom method: Derivation and application to impurities, surfaces, and other defects in metals, Phys Rev B 29 (1984) 6443, https://doi.org/10.1103/PhysRevB.29.6443.
[38] D. Farkas, A. Caro, Model interatomic potentials and lattice strain in a high-entropy alloy, J Mater Res 33 (2018) 3218–3225, https://doi.org/10.1557/JMR.2018.245.
[39] S. Guo, Q. Hu, C. Ng, C.T. Liu, More than entropy in high-entropy alloys: Forming solid solutions or amorphous phase, Intermetallics (Barking) 41 (2013) 96–103, https://doi.org/10.1016/J.INTERMET.2013.05.002.
[40] Y. Mishin, D. Farkas, M.J. Mehl, D.A. Papaconstantopoulos, Interatomic potentials for monoatomic metals from experimental data and *ab initio* calculations, Phys Rev B 59 (1999) 3393, https://doi.org/10.1103/PhysRevB.59.3393.
[41] C. Varvenne, A. Luque, W.G. Nöhring, W.A. Curtin, Average-atom interatomic potential for random alloys, Phys Rev B 93 (2016), 104201, https://doi.org/10.1103/PhysRevB.93.104201.
[42] A.P. Thompson, H.M. Aktulga, R. Berger, D.S. Bolintineanu, W.M. Brown, P. S. Crozier, P.J. In 't Veld, A. Kohlmeyer, S.G. Moore, T.D. Nguyen, R. Shan, M. J. Stevens, J. Tranchida, C. Trott, S.J. Plimpton, LAMMPS - a flexible simulation tool for particle-based materials modeling at the atomic, meso, and continuum scales, Comput Phys Commun 271 (2022), 108171, https://doi.org/10.1016/J.CPC.2021.108171.
[43] R. Nikbakht, M. Saadati, T.S. Kim, M. Jahazi, H.S. Kim, B. Jodoin, Cold spray deposition characteristic and bonding of CrMnCoFeNi high entropy alloy, Surf Coat Technol 425 (2021), 127748, https://doi.org/10.1016/J.SURFCOAT.2021.127748.
[44] S. Zhang, C.L. Wu, C.H. Zhang, Phase evolution characteristics of FeCoCrAlCuVxNi high entropy alloy coatings by laser high-entropy alloying, Mater Lett 141 (2015) 7–9, https://doi.org/10.1016/J.MATLET.2014.11.017.
[45] T. Schneider, E. Stoll, Molecular-dynamics study of a three-dimensional one-component model for distortive phase transitions, Phys Rev B 17 (1978) 1302, https://doi.org/10.1103/PhysRevB.17.1302.
[46] K. Meyer, I.K. Schuller, C.M. Falco, Thermalization of sputtered atoms, J Appl Phys 52 (1981) 5803–5805, https://doi.org/10.1063/1.329473.
[47] A. Stukowski, Visualization and analysis of atomistic simulation data with OVITO-the Open Visualization Tool, Model Simul Mat Sci Eng 18 (2010), 015012, https://doi.org/10.1088/0965-0393/18/1/015012.
[48] J.D. Honeycutt, H.C. Andersen, Molecular dynamics study of melting and freezing of small Lennard-Jones clusters, Journal of Physical Chemistry 91 (1987) 4950–4963, https://doi.org/10.1021/j100303a014.
[49] H. Köstenbauer, G.A. Fontalvo, M. Kapp, J. Keckes, C. Mitterer, Annealing of intrinsic stresses in sputtered TiN films: The role of thickness-dependent gradients of point defect density, Surf Coat Technol 201 (2007) 4777–4780, https://doi.org/10.1016/J.SURFCOAT.2006.10.017.
[50] S. Chakravarty, M. Jiang, U. Tietze, D. Lott, T. Geue, J. Stahn, H. Schmidt, Migration and annihilation of non-equilibrium point defects in sputter deposited nanocrystalline alpha-Fe films, Acta Mater 59 (2011) 5568–5573, https://doi.org/10.1016/J.ACTAMAT.2011.05.029.
[51] L. Velasco, A.M. Hodge, Growth twins in high stacking fault energy metals: Microstructure, texture and twinning, Materials Science and Engineering: A 687 (2017) 93–98, https://doi.org/10.1016/J.MSEA.2017.01.065.
[52] L. Velasco, M.N. Polyakov, A.M. Hodge, Influence of stacking fault energy on twin spacing of Cu and Cu–Al alloys, Scr Mater 83 (2014) 33–36, https://doi.org/10.1016/J.SCRIPTAMAT.2014.04.002.
[53] S.P. Coleman, D.E. Spearot, L. Capolungo, Virtual diffraction analysis of Ni [0 1 0] symmetric tilt grain boundaries, Model Simul Mat Sci Eng 21 (2013), 055020, https://doi.org/10.1088/0965-0393/21/5/055020.
[54] S. Guo, C.T. Liu, Phase stability in high entropy alloys: Formation of solid-solution phase or amorphous phase, Progress in Natural Science: Materials International 21 (2011) 433–446, https://doi.org/10.1016/S1002-0071(12)60080-X.
[55] X. Yang, Y. Zhang, Prediction of high-entropy stabilized solid-solution in multi-component alloys, Mater Chem Phys 132 (2012) 233–238, https://doi.org/10.1016/J.MATCHEMPHYS.2011.11.021.
[56] M.G. Poletti, L. Battezzati, Electronic and thermodynamic criteria for the occurrence of high entropy alloys in metallic systems, Acta Mater 75 (2014) 297–306, https://doi.org/10.1016/J.ACTAMAT.2014.04.033.
[57] Z.S. Nong, J.C. Zhu, Y. Cao, X.W. Yang, Z.H. Lai, Y. Liu, Stability and structure prediction of cubic phase in as cast high entropy alloys, Materials Science and Technology 30 (2014) 363–369, https://doi.org/10.1179/1743284713Y.0000000368.
[58] A. Takeuchi, A. Inoue, Classification of Bulk Metallic Glasses by Atomic Size Difference, Heat of Mixing and Period of Constituent Elements and Its Application to Characterization of the Main Alloying Element, Mater Trans 46 (2005) 2817–2829, https://doi.org/10.2320/MATERTRANS.46.2817.
[59] Y.C. Hsu, C.L. Li, C.H. Hsueh, Effects of Al Addition on Microstructures and Mechanical Properties of CoCrFeMnNiAlx High Entropy Alloy Films, Entropy 22 (2019) 2, https://doi.org/10.3390/E22010002.
[60] Z. Tang, M.C. Gao, H. Diao, T. Yang, J. Liu, T. Zuo, Y. Zhang, Z. Lu, Y. Cheng, Y. Zhang, K.A. Dahmen, P.K. Liaw, T. Egami, Aluminum alloying effects on lattice types, microstructures, and mechanical behavior of high-entropy alloys systems, JOM 65 (2013) 1848–1858, https://doi.org/10.1007/s11837-013-0776-z.
[61] S. Gao, T. Kong, M. Zhang, X. Chen, Y.W. Sui, Y.J. Ren, J.Q. Qi, F.X. Wei, Y.Z. He, Q.K. Meng, Z. Sun, Effects of titanium addition on microstructure and mechanical properties of CrFeNiTix (x = 0.2–0.6) compositionally complex alloys, J Mater Res 34 (2019) 819–828, https://doi.org/10.1557/JMR.2019.40.
[62] X. Wang, H. Xie, L. Jia, Z. Lu, Effect of Ti, Al and Cu addition on structural evolution and phase constitution of FeCoNi system equimolar alloys, in: Materials Science Forum, Trans Tech Publications Ltd, 2012: pp. 335–338. doi:10.4028/www.scientific.net/MSF.724.335.
[63] Z. Wu, H. Bei, F. Otto, G.M. Pharr, E.P. George, Recovery, recrystallization, grain growth and phase stability of a family of FCC-structured multi-component equiatomic solid solution alloys, Intermetallics (Barking) 46 (2014) 131–140, https://doi.org/10.1016/J.INTERMET.2013.10.024.
[64] Z. An, H. Jia, Y. Wu, P.D. Rack, A.D. Patchen, Y. Liu, Y. Ren, N. Li, P.K. Liaw, Solid-solution CrCoCuFeNi high-entropy alloy thin films synthesized by sputter deposition, Mater Res Lett 3 (2015) 203–209, https://doi.org/10.1080/21663831.2015.1048904.
[65] J.W. Yeh, S.J. Lin, M.H. Tsai, S.Y. Chang, High-entropy coatings, in: High-Entropy Alloys, Springer International Publishing (2016) 469–491, https://doi.org/10.1007/978-3-319-27013-5_14.
[66] B. Fultz, Effects of Diffusion and Nucleation on Phase Transformations, in: Phase Transitions in Materials, Cambridge University Press, 2020: pp. 109–130. doi:10.1017/9781108641449.007.
[67] S.S. Lin, J.L. Huang, P. Šajgalik, Effects of substrate temperature on the properties of heavily Al-doped ZnO films by simultaneous r.f. and d.c. magnetron sputtering, Surf Coat Technol 190 (2005) 39–47, https://doi.org/10.1016/J.SURFCOAT.2004.03.022.
[68] J. Yang, Y. Huang, K. Xu, Effect of substrate on surface morphology evolution of Cu thin films deposited by magnetron sputtering, Surf Coat Technol 201 (2007) 5574–5577, https://doi.org/10.1016/J.SURFCOAT.2006.07.227.
[69] J. Shi, D. Kojima, M. Hashimoto, The interaction between platinum films and silicon substrates: Effects of substrate bias during sputtering deposition, J Appl Phys 88 (2000) 1679, https://doi.org/10.1063/1.373871.
[70] C. Li, M. Furuta, T. Matsuda, T. Hiramatsu, H. Furuta, T. Hirao, Effects of substrate on the structural, electrical and optical properties of Al-doped ZnO films prepared

by radio frequency magnetron sputtering, Thin Solid Films 517 (2009) 3265–3268, https://doi.org/10.1016/J.TSF.2008.11.103.